Project No. 15-8243

Radiation-induced Swelling and Microcracking in SiC Cladding for LWRs

Fuel Cycle Research and Development

Izabela Szlufarska
University of Wisconsin, Madison

Collaborators
University of Florida

Frank Goldner, Federal POC
Yutai Katoh, Technical POC

NEUP Nuclear Energy University Programs
U.S. Department of Energy

Final Report

Project Title:	**Radiation-induced swelling and microcracking in SiC cladding for LWRs**	
Covering Period:	10/1/2015 – 3/31/2019	
Date of Report:	7/17/2019	
Recipient:	University of Wisconsin Madison, WI 53706	
Project number: **Project Number:**	DE-NE0008418 15-8243	
Subcontractors:	University of Florida	
Other Partners:	N/A	
Contact(s):	Principal Investigator:	Izabela Szlufarska szlufarska@wisc.edu
	Co-Principal Investigators:	Paul Voyles (voyles@engr.wisc.edu) Michael Tonks (michael.tonks@ufl.edu)

Table of Content

1 Introduction **3**

2 Phase field model of microcracking **4**

2.1 Introduction ***4***

2.2 Phase field fracture model including anisotropic elasticity ***5***

2.2.1 Phase field fracture model including anisotropic elasticity *5*

2.2.2 Strain energy decomposition *6*

2.2.3 Governing equations *6*

2.2.4 Numerical examples *7*

2.3 Anisotropic fracture energy ***10***

2.3.1 Anisotropic fracture energy model and governing equations *10*

2.3.2 Numerical examples *11*

2.4 Application to SiC ***14***

3 Traction-separation curves for grain boundary (GB) fracture **16**

4 Prediction of radiation-induced swelling **20**

5 Mechanical properties of unirradiated and irradiated SiC **24**

5.1 Sample fabrication and experimental methods ***24***

5.2 *In situ* nanoindentation studies on as-synthesized 3C-SiC ***25***

5.3 *In situ* nanoindentation studies on irradiated 3C-SiC ***27***

5.4 *Ex situ* nanoindentation studies ***29***

6 Summary **30**

7 Conference presentations **30**

8 Publications **31**

9 References **32**

1 Abstract

After the Fukushima accident in 2011, SiC has attracted considerable attention as a potential material for fuel cladding that can offer increased accident tolerance in light water reactors (LWRs) compared to zircaloy cladding. Existing measurements on nuclear grade SiC/SiC composites made of high-purity, stoichiometric SiC have already shown very good radiation tolerance in various harsh environments. However, there are a number of challenges that need to be addressed before SiC composites can be successfully used in LWR technologies. One of them is irradiation-induced swelling, which can lead to development of significant stresses in the matrix, followed by microcracking and subsequent release of fission products. Models of irradiation-induced swelling had been largely empirical and therefore they cannot be used to predict the microstructural dependence of microcracking. Existing models are also limited by the lack of understanding of defects that form due to irradiation in the range of temperatures relevant to fuel cladding in LWRs (<1000°C). Many of the defects in this regime of temperature are too small to be detected with traditional transmission electron microscopy (TEM) techniques. In fact the defects observed in traditional TEM account only for 10-45% of the swelling measured in irradiated SiC. Here, we developed a multi-scale simulation methodology combined with state of the art experimental imaging techniques based on aberration corrected scanning transmission electron microscopy (STEM) to provide a scientific basis for predictive models of radiation swelling and microcracking in SiC.

Specifically, we have developed a phase field fracture model that predicts microcrack initiation and growth in polycrystalline SiC. The model accounts for single crystal anisotropy, including anisotropy in the elastic constants and anisotropic surface energy. It also considers the reduced fracture strength of grain boundaries. The model was implemented using the MARMOT mesoscale nuclear materials tool. We have parameterized the model for SiC using molecular dynamics simulation results. The model has been verified using single crystal, bicrystal, and polycrystal examples.

Swelling model has also been developed based on cluster dynamics simulations of defect evolution in SiC. We found that point defects and small defect clusters have a significant contribution to swelling. This finding is important because point defects and very small defect clusters are not visible in experiments (e.g., in TEM). Combined modeling and experiments can bring critical insights into how swelling depends on irradiation conditions and the microstructure.

In situ nanoindentation tests and *ex situ* nanoindentation tests were performed on as-synthesized 3C-SiC and 3C-SiC irradiated under different radiation conditions. Without radiation, bend contour movement and residual bend contours after indentation demonstrate some room-temperature plastic flow and residual plastic deformation. Plastic deformation recovery is also observed on unirradiated samples during unloading. Radiation-induced embrittlement is demonstrated by differences in crack geometry in *in situ* tests, and is consistent with *ex situ* test results. Failure by single, straight, cracks indicates decreased fracture toughness due to irradiation in 3C-SiC.

Future work includes coupling of the swelling and fracture models and development of a master equation that can be used in the BISON code.

2 Introduction

The objectives of the project were

1. Develop continuum models of swelling with parameters informed by atomistic simulations and experiments. Determine how irradiation-induced defects contribute to swelling.
2. Develop a microstructure-informed mesoscale model for fracture of SiC.
3. Integrate the model of swelling with mesoscale model of fracture to predict the effect of swelling on fracture in irradiated SiC and derive a master equation that can be used as in put for BISON code.

We have met objectives 1 and 2, which is development of models for swelling and for microcracking in SiC, respectively. We have not yet integrated the two parts of the model (objectives 3) because it took longer than expected to parameterize and validated each of the individual models.

This report is structured as follows. In section 2 we report on developments of phase field model of microcracking that includes anisotropic elastic properties and anisotropic fracture. In Section 3 we provide parameters for the models determined from atomistic simulations. In section 4 we report on a model of swelling, which is based on cluster dynamics technique and which is built on parameters determined both from atomistic simulations and from experiments. Validation for the model is provided using experimental STEM and TEM studies. In section 5 we report on *in situ* and *ex situ* experimental studies of mechanical properties of unirradiated and irradiated SiC.

3 Phase field model of microcracking

3.1 Introduction

Silicon carbide has been considered as a potential alternative cladding material for zirconium-based alloys because of its better mechanical and thermal behaviors. However, brittleness can be a major problem for SiC claddings compared to Zr alloys, due to the strong covalent Si-C bonds. The most commonly used SiC cladding has a zinc-blende (3C) structure which consists of two interpenetrating face-centered cubic (fcc) lattices [1]. 3C-SiC shows strong anisotropy in both the elasticity tensor and the fracture energy.

In general, there are two common fracture types in brittle crystalline structures. One is transgranular fracture, where the crack propagates through the interior of a grain. The other type is intergranular fracture, where the crack propagates along the grain boundaries (GBs); this occurs when the GBs are sufficiently weak to compensate for the extra energy consumed in deflecting the crack. There are many factors that could influence how cracks propagate in a crystalline structure, such as grain size, porosity, and temperature [2].

Due to the great potential of silicon carbide as a cladding material, many SiC composites have been developed and tested experimentally and numerically [3, 4]. For instance, scanning electron microscopy (SEM) was used to study the micro-crack behaviors and mirror-like, clean, and plain-cleavage of large grains were all found in an unirradiated sample. Irradiated specimens were shown significant changes in statistical flexural strength, which was attributed to an

enhanced cleavage resistance (increased transgranular cleavage energy) and the corresponding changes in crack initiation [5].

Numerical studies of crack behaviors of SiC can be very valuable in establishing how fracture depends on the details of the inherent microstructure, radiation-induced defects, and temperature. Such models need to consider the single crystal anisotropy of SiC, as well as the impact of the grain structure. Traditional models are based on the finite element technique, but they can be numerically prohibitive for complex 3D microstructures. Finite element-based fracture mechanics methods model crack as a sharp interface. In contrast, the phase field method is based on a diffuse-interface description of cracks, which is relatively easy to implement and solve. However, up to date there have been no well-developed phase field fracture models that can consider the single crystal anisotropy. Thus, our goal is to develop a phase field fracture model that can both capture the elastic anisotropy of SiC as well as the anisotropy of the fracture energy.

In the following sections, we discuss developments of a mesoscale model that includes anisotropic elasticity and fracture energy. Subsequently, based on molecular dynamics (MD) simulation results, we worked out the first step of fracture simulations of SiC, where a polycrystal fracture simulation was done based on our model.

3.2 Phase field fracture model including anisotropic elasticity

Numerical simulations of fracture in solids often consider sharp cracks. The phase field fracture method was first developed by Francfort [6] and Bourdin [7]. It provides a continuous description of fracture and is a powerful tool for modeling fracture because it can both determine the crack path and represent the creation of new free surfaces. To prevent compressive stress from causing crack propagation, Amor *et al.* [8] separated the strain energy density function into hydrostatic and deviatoric parts. Subsequently, Miehe *et al*. [9] proposed one of the most influential phase field fracture models in isotropic materials by splitting the strain energy density into tensile and compressive parts, where only the tensile energy density contributes to crack propagation. However, all these models have assumed isotropic properties of materials.

In this section, a new phase field fracture model for brittle materials is proposed that considers elastic anisotropy. Specifically, this model decomposes the strain energy density function into positive and negative parts, which correspond to tensile and compressive stress tensors, respectively. By considering elastic anisotropy, the model accounts for stresses induced by the misorientation between grains.

3.2.1 Phase field fracture model including anisotropic elasticity

Different from traditional discrete description of sharp cracks, phase field models apply a diffuse-interface description of a crack, which is based on a continuous variable d ranging from 0 to 1. The value $d = 0$ indicates intact material, $d = 1.0$ indicates a fully cracked specimen, and the material is considered damaged when $0 < d < 1.0$. The total potential energy of a cracked brittle material is defined as a sum of elastic energy and crack surface energy. The fracture energy was developed as a volume integral by Bourdin *et al.* [6] and then used by Miehe [9]. The strain

energy is decomposed to exclude the contribution of compressive stress on crack propagation, so that

$$F = \int_{\Omega} \left\{ ((1-d)^2(1-k)+k)\psi^+ + \psi^- + g_c \left(l\nabla^2 d + \frac{d^2}{2l} \right) \right\} \mathrm{d}\Omega \tag{1}$$

where ψ^+ represents the positive part of strain energy, which corresponds to the strain energy by tensile stress, and ψ^- represents the negative part of strain energy.

3.2.2 Strain energy decomposition

As we are considering only brittle materials, it is reasonable to assume small deformation, so that the strain tensor can be defined as

$$\boldsymbol{\epsilon} = \frac{1}{2}(\nabla \boldsymbol{u} + \nabla \boldsymbol{u}^{\boldsymbol{T}}).$$

We also assume a linear elastic material response, so that the stress tensor of the unbroken material

$$\boldsymbol{\sigma_0} = \mathbb{C}\boldsymbol{\epsilon}, \tag{3}$$

where $\mathbb{C}$ is the fourth order elasticity tensor, and spectral decomposition is applied to obtain the tensile and compressive parts of the stress tensor. Here

$$\boldsymbol{\sigma_0} = \mathbb{C}\boldsymbol{\epsilon} = \boldsymbol{Q\Lambda Q^T} = \boldsymbol{Q}(\boldsymbol{\Lambda}^+ + \boldsymbol{\Lambda}^-)\boldsymbol{Q^T} = \boldsymbol{\sigma}^+ + \boldsymbol{\sigma}^-, \tag{4}$$

where $\boldsymbol{Q}$ is the eigenvector matrix, $\boldsymbol{\Lambda} = diag(\lambda_1, \lambda_2, \lambda_3)$ is the diagonal eigenvalue matrix, and $\boldsymbol{\Lambda}^+ = \frac{1}{2}(|\boldsymbol{\Lambda}| + \boldsymbol{\Lambda})$ and $\boldsymbol{\Lambda}^- = \frac{1}{2}(\boldsymbol{\Lambda} - |\boldsymbol{\Lambda}|)$ represent the positive and negative diagonal eigenvalue matrices, respectively. Based on the spectral decomposition, the tensile and compressive stress tensor are defined as

$$\boldsymbol{\sigma}^+ = \boldsymbol{Q\Lambda}^+\boldsymbol{Q^T} \tag{5}$$

$$\boldsymbol{\sigma}^- = \boldsymbol{Q\Lambda}^-\boldsymbol{Q^T} \tag{6}$$

and the positive and negative parts of strain energy are then defined as

$$\psi^+ = \frac{1}{2}\boldsymbol{\sigma}^+ : \boldsymbol{\epsilon} \tag{7}$$

$$\psi^- = \frac{1}{2}\boldsymbol{\sigma}^- : \boldsymbol{\epsilon} \tag{8}$$

Thus, the total free energy in a damaged material is defined as,

$$F = \int_{\Omega} \left\{ ((1-d)^2(1-k)+k)\psi^+ + \psi^- + g_c \left(l\nabla^2 d + \frac{d^2}{2l} \right) \right\} d\Omega \tag{9}$$

3.2.3 Governing equations

Based on the total free energy obtained in the previous section, the stress tensor in a damaged material can be found as

$$\boldsymbol{\sigma} = \frac{\partial F}{\partial \boldsymbol{\epsilon}} = ((1-d)^2(1-k)+k)\frac{\partial \psi^+}{\partial \boldsymbol{\epsilon}} + \frac{\partial \psi^-}{\partial \boldsymbol{\epsilon}} = ((1-d)^2(1-k)+k)\boldsymbol{\sigma}^+ + \boldsymbol{\sigma}^-, \tag{10}$$

where a specific process of positive stress tensor derivation is

$$\frac{\partial \psi^+}{\partial \epsilon} = \frac{1}{2}\frac{\partial \boldsymbol{\sigma}^+}{\partial \boldsymbol{\sigma}}\frac{\partial \boldsymbol{\sigma}}{\partial \boldsymbol{\epsilon}} : \boldsymbol{\epsilon} + \frac{1}{2}\boldsymbol{\sigma}^+\mathbb{I} = \frac{1}{2}\mathbb{P}^+\mathbb{C}\epsilon + \frac{1}{2}\boldsymbol{\sigma}^+ = \frac{1}{2}\mathbb{P}^+\boldsymbol{\sigma_0} + \frac{1}{2}\boldsymbol{\sigma}^+ = \boldsymbol{\sigma}^+. \tag{11}$$

Thus, the equilibrium equation can be written

$$\nabla \cdot \left[((1-d)^2 + k) \frac{\partial \psi_0^+}{\partial \epsilon} + \frac{\partial \psi_0^-}{\partial \epsilon} \right] = 0. \tag{12}$$

The other governing equation, the phase field evolution equation, can also be found

$$\frac{\partial d}{\partial t} = -L \frac{\delta F}{\delta d} = -L \left(-2(1-d) H_0^+ + \frac{g_c}{l} d - g_c l \nabla^2 \mathrm{d} \right). \tag{13}$$

3.2.4 Numerical examples

Since SiC is an fcc material, the first numerical example is the mode I fracture simulation of fcc materials, where the geometry and boundary conditions are shown in Figure 2.1, and the material properties are shown in Table 2.1.

Table 2.1. Material properties used in mode I fracture simulation

$C_{11}(GPa)$	$C_{12}(GPa)$	$C_{44}(GPa)$	$l(mm)$	$g_c(GPa \cdot mm)$	$\eta(s/mm)$
127.0	70.8	73.55	0.01	1.0×10^{-3}	1.0×10^{-6}

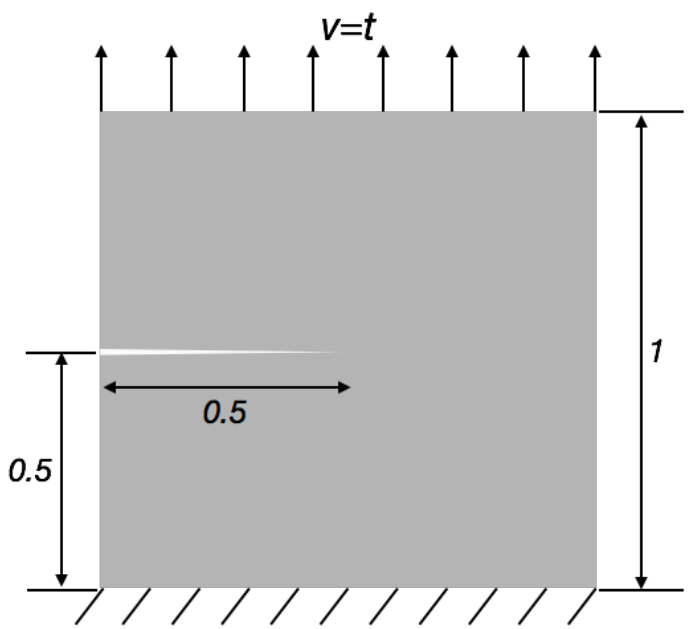

Figure 2.1. Geometry and boundary conditions used in Mode I fracture simulation

Five 2D cases in which the planar crystal orientations range from 0° to 90° are carried out, and the resultant crack path and stress strain curves are shown in Figure 2.2.

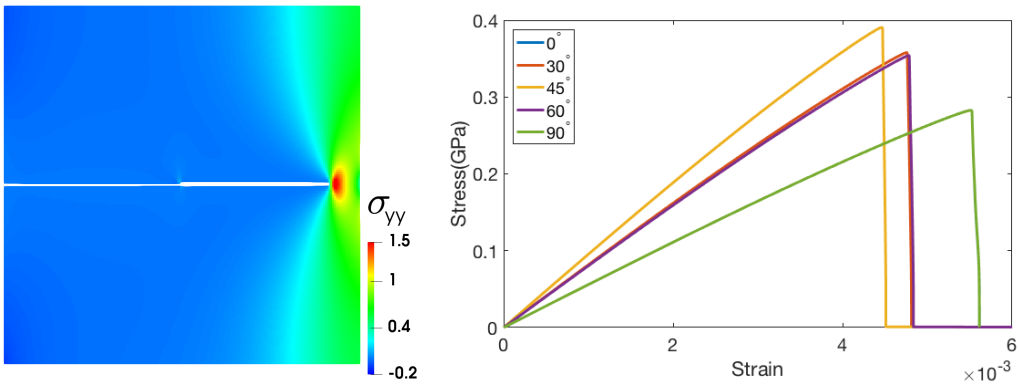

(a)Crack path and stress distribution. (b) Stress-strain curves

Figure 2.2 Stress-strain curves in the mode I fracture simulation of fcc crystal, including elastic anisotropy.

From Figure 2.2b we can see that the slope of the stress-strain curves varies with the crystal orientation. Also, overlapping slopes of 30° and 60° as well as 0° and 90° are clearly shown in the plot, which demonstrates that our model captures the cubic symmetry of the material.

A more complex numerical example of polycrystalline sample has also been studied by including the anisotropic elasticity tensor. The sample contains 36 grains with a side length of 1 mm and with random orientations ranging from 0° to 90°. Three different sets of crystal orientations are shown in Figure 2.3(a-c), and the corresponding influence of crystal orientations on the elasticity tensor is shown in Figure 2.3(d-f), where one component of the elasticity tensor is used for comparison.

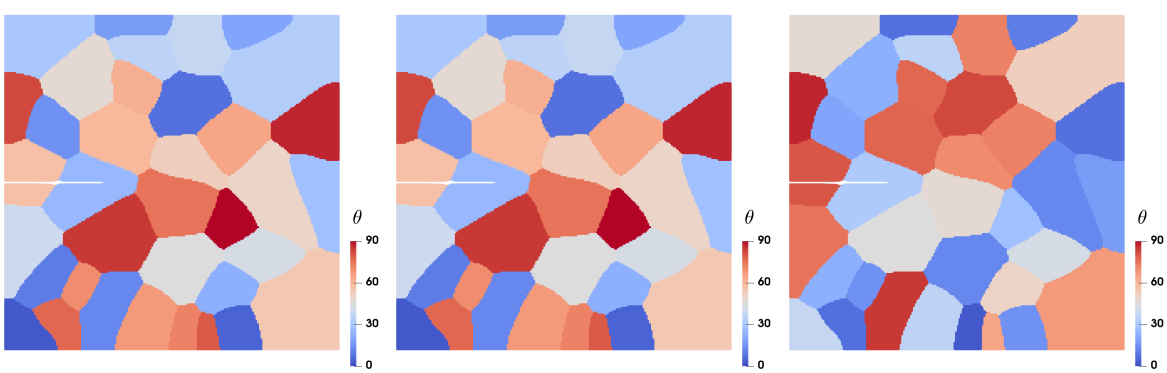

(a) crystal orientation 1 (b) crystal orientation 2 (c) crystal orientation 3

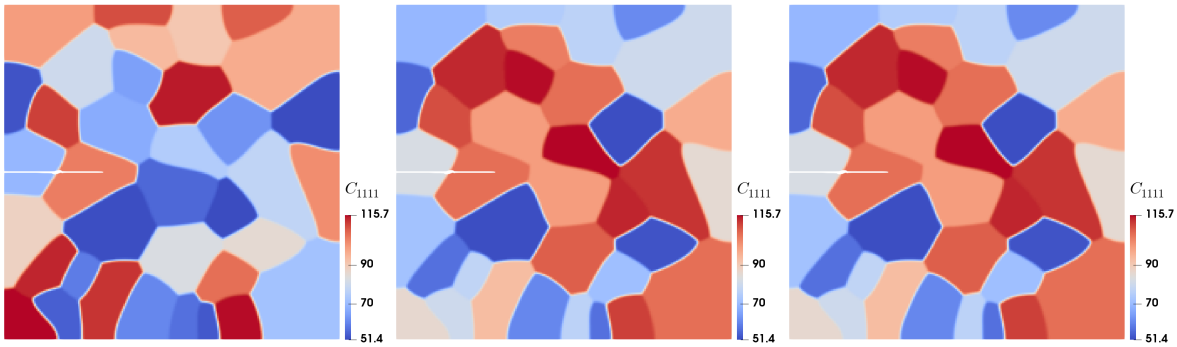

(d) C_{1111} for orientation 1 (e) C_{1111} for orientation (f) C_{1111} for orientation 3

Figure 2.3. The three polycrystalline textures used as examples, where (a) – (c) show the planar crystal orientations of the 36 grain polycrystalline structure and (d) – (f) show the corresponding changes in the C_{1111} component of the elasticity tensor.

The σ_{yy} stress field and crack path for the three polycrystals are shown in Figures 2.4(a-c). Though each crack propagates in a similar manner, the impact of the different crystal orientations is evident. The stress-strain curves, which are shown in Figure 2.4d, more clearly illustrate the impact of the different crystal orientations on the polycrystalline fracture.

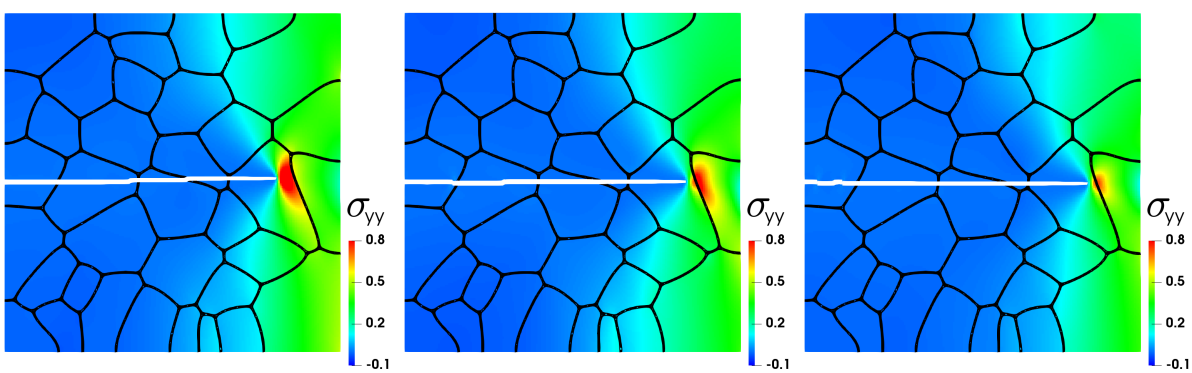

(a) case I at 7.13 ms (b) case II at 7.93 ms (c) case II at 7.09 ms

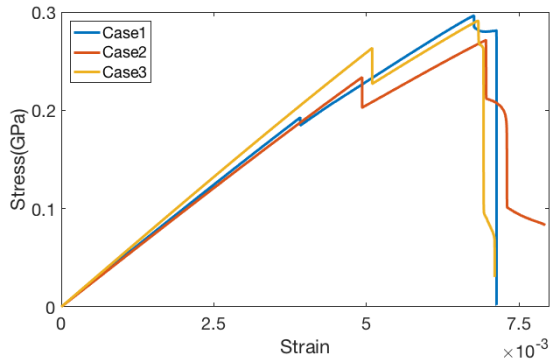

(d) Stress-strain curves obtained in three cases

Figure 2.4. Fracture results from the three polycrystalline textures, in which (a) – (c) show the crack paths and yy-component of the stress tensor and (d) shows the three strain-strain curves, which vary due to the different crystal orientations.

As we can see from Figure 2.4, the different crystal orientations do not significantly impact the crack path (although small changes are present). However, they have a large impact on the stress field and on the stress-strain curves. Only straight crack paths are obtained in these three simulations, since we only include elastic anisotropy. In real materials, in which the fracture energy is also anisotropic, we would expect more significant changes in the crack paths due to the crystal orientations.

3.3 Anisotropic fracture energy

A couple of phase field models have been developed to capture the anisotropy of the fracture energy, though most of them assume isotropic elasticity in their work. Li *et al.* [10] developed a phase field model that includes a strongly anisotropic fracture energy with a Taylor series expansion of the fracture energy, where a rank two or rank four tensor parameters are used to describe the anisotropy of fracture energy. However, this model does not avoid the contribution of compressive stress on crack propagation. Teichtmeister *et al.* [11] built rank-four and rank-two tensors to represent the anisotropic fracture energies in different anisotropic materials, but the model assumed isotropic elasticity. To our knowledge, there is currently no phase field fracture model that considers the fracture energy to be dependent on the creation of new crack surface, i.e, the out normal vector of the crack surface, and that therefore would account for anisotropic fracture energy.

3.3.1 Anisotropic fracture energy model and governing equations

In our model, the impact of surface energy anisotropy is introduced using a parameter κ, which is dependent on the out normal vector of the crack surface, $\vec{n} = \frac{\nabla d}{|\nabla d|} = \frac{d_x\vec{\boldsymbol{i}}+d_y\vec{\boldsymbol{j}}+d_z\vec{\boldsymbol{k}}}{\sqrt{d_x^2+d_y^2+d_z^2}}$, where

$\nabla d = (d_x, d_y, d_z) = \left(\frac{\partial d}{\partial x}, \frac{\partial d}{\partial y}, \frac{\partial d}{\partial z}\right)$. A general mode-2 anisotropic fracture energy with the weakest crack preference direction along the y-z plane is defined by

$$\kappa(d_x, d_y, d_z) = \begin{cases} \left(1 + \delta \frac{(d_x^2 - d_y^2)}{d_x^2 + d_y^2}\right)^n & 2D \\ \left(1 + \delta \frac{(d_x^2 + d_z^2 - d_y^2)}{d_x^2 + d_y^2 + d_z^2}\right)^n & 3D \end{cases} \quad (15)$$

where n is the order number. In order to obtain change in the weakest fracture direction, the out-normal vector $\vec{n}$ is rotated using a rotation matrix, so that

$$[d_x', d_y', d_z']' = R_x(\alpha_0) R_y(\beta_0) R_z(\theta_0) [d_x, d_y, d_z]', \quad (16)$$

where $\alpha_0, \beta_0, \theta_0$ are the rotation angles along the x-axis, y-axis and z-axis, respectively. Thus, the total free energy is defined as,

$$F = \int_\Omega \left\{ ((1-d)^2(1-k) + k)\psi^+ + \psi^- + g_c \left(\kappa(\vec{n}) \frac{l}{2} \nabla^2 d + \frac{d^2}{2l} \right) \right\} d\Omega \quad (17)$$

The phase field crack evolution governing equation is given by

$$\frac{\partial d}{\partial t} = -L \left(-2(1-d)H_0^+ + \frac{g_c}{l} d - g_c l \kappa \nabla^2 \mathrm{d} - \frac{\partial \kappa}{\partial \nabla d} \frac{g_c l}{2} |\nabla d|^2 \right). \quad (18)$$

3.3.2 Numerical examples

Firstly, the impact of the anisotropy strength δ on the crack path was investigated, using δ values ranging from 0.1 to 0.9 with a uniform interval of 0.1 and one additional case of 0.95, which is close to 1. Also, two reference angles of $\theta_0 = 30°$ and $\theta_0 = 45°$ were studied. The order number was fixed with n = 2. Mode I fracture simulations were performed, where the geometry and boundary conditions were the same as shown in Figure 2.1. The parameters l, g_c, η were set as 5×10^{-3}mm, 1×10^{-3}GPa · mm, 1×10^{-6}s/mm, respectively. Adaptive mesh with a minimum mesh size level of $h = \frac{l}{2}$ was applied on the geometry and the specific adaptive mesh strategy can be found in MOOSE website. The time step size was $\mathrm{d}t = 3\times10^{-6}$ ms. The resultant crack angles for cases $\theta_0 = 30°$ and $\theta_0 = 45°$, corresponding to different anisotropic strengths, are shown in Figures 2.5a and 2.5b, respectively. As shown in the figure, the crack angles approached θ_0 with increasing θ_0 value, while the maximum crack angle was around 25° for $\theta_0 = 30°$ and 38° for $\theta_0 = 45°$, and the crack angle reaches the maximum and stays the same when the δ is greater than 0.7. Thus, θ_0 dictates the preferred fracture direction, but the values of δ define the strength of the preference. The stress strain curves, shown in Figures 2.5c and 2.5d indicate that the maximum crack stress decreases as δ increases.

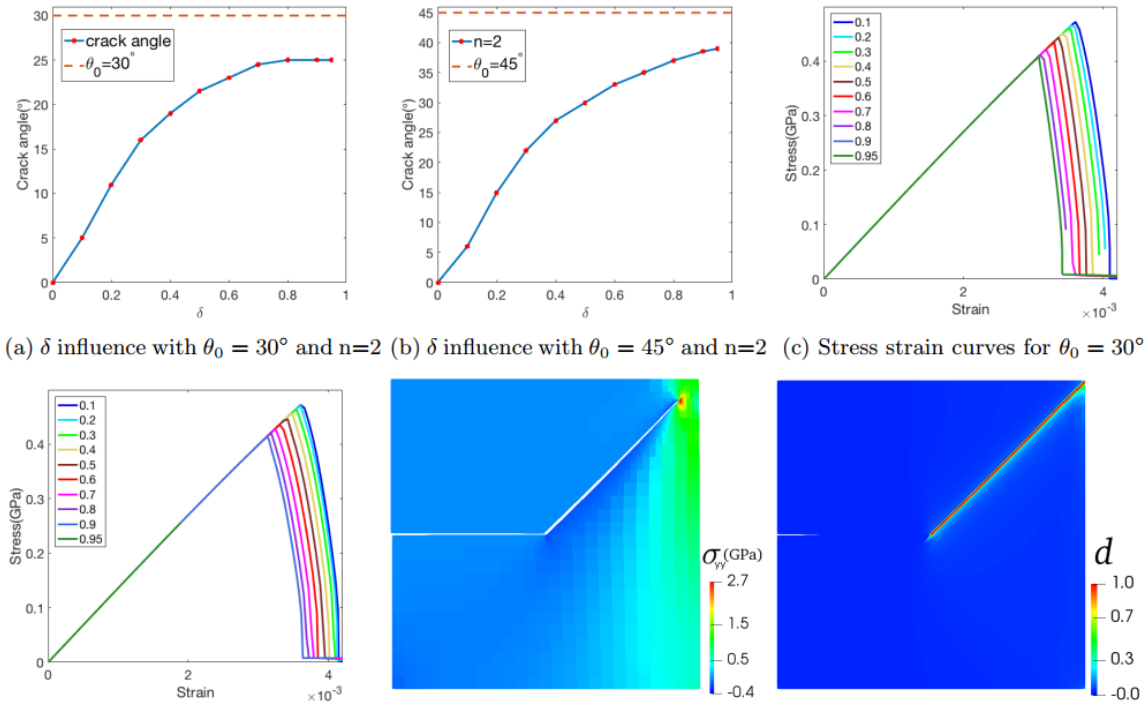

(a) δ influence with $\theta_0 = 30°$ and n=2 (b) δ influence with $\theta_0 = 45°$ and n=2 (c) Stress strain curves for $\theta_0 = 30°$

(d) Stress strain curves for $\theta_0 = 45°$ (e) n=4 and $\delta = 0.95$ for $\theta_0 = 45°$ (f) Crack path for $\theta_0 = 45°$

Figure 2.5. The impact of the anisotropic strength δ on crack propagation in single crystal mode I fracture simulations with n = 2, where (a) and (b) plot the angle of the actual crack for $\theta_0 = 30°$ and $\theta_0 = 45°$, respectively, (c) and (d) show the stress strain curves for the two angles, (e) shows the crack path and stress field before the sample is fully cracked and (f) shows the final crack path for the simulation from (e).

The second example conducted is a 3D crack example, where isotropic elasticity tensor is assumed. A Mode I fracture simulation in 3D is carried out, where the geometry is the same as shown in Figure 2.1 with a thickness of 0.02 mm along the z-direction, and the elasticity properties picked are $\lambda = 120\text{GPa}, \mu = 80\text{GPa}$. A length parameter $l = 0.01$ mm is set and a uniform mesh of 5×10^{-3} mm is used. The anisotropic rotation angles are set ranging from $\theta_z = -45°$ to $\theta_z = 45°$, with an interval of $\Delta\theta_z = 15°$. The anisotropy strength $\delta = 0.4$. The resultant crack paths are shown in Figure 2.6.

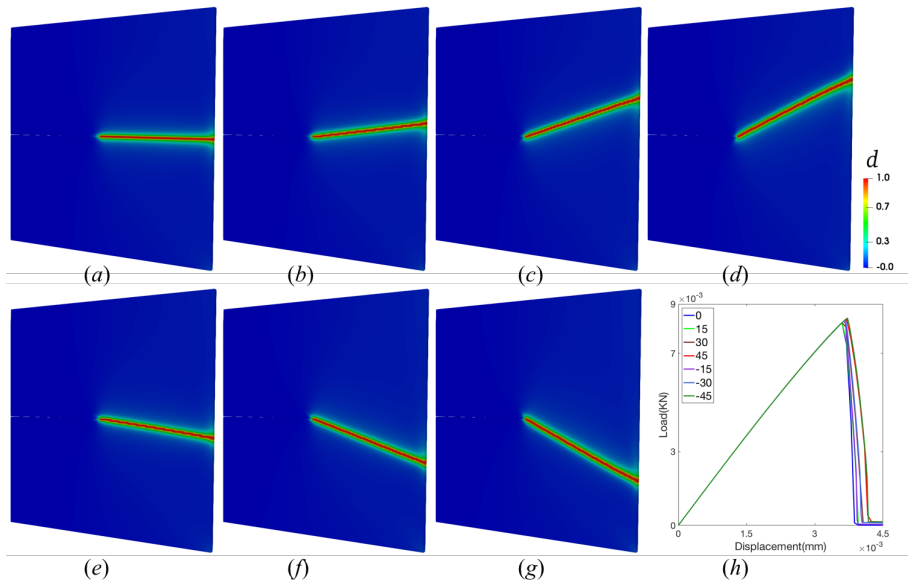

Figure 2.6. The impact of crystal orientation θ on the crack propagation of Mode I fracture simulations in 3D using isotropic elasticity and anisotropic fracture energy, with $l = 0.01\ mm$, δ = 0.4, n = 2, and reference angles ranging from -45◦ to 45◦ with an interval of 15◦. The final crack paths for different reference angles shown in (a) - (g), and the resultant stress-strain curves are shown in (h).

As a final application of this model, we consider a polycrystalline sample in order to determine the influence of crystal orientations on the final crack path and on the stress-strain curves. The anisotropies were considered for both the elasticity tensor and the fracture energy to simulate Mode I fractures in polycrystalline samples. Specifically, a 1 mm × 1 mm polycrystal structure with 16 grains was prepared with different crystal orientations, impacting both the elasticity tensor and the fracture energy. Three different sets of randomly rotated crystal orientations ranging from $-90°$ to $90°$ around the *z*-axis were picked for the study, as shown in Figure 2.7(a)-(c). The crack thickness parameter is set as l = 0.01mm, a uniform mesh size of $h = 5\times10^{-3}$mm is used in the simulations, and the material properties are shown in Table 2.1. The displacement load was applied along the *y*-direction was applied on the top side and the displacement is a linear function of time. On the bottom side we used fixed displacement conditions. The polycrystal had an initial horizontal crack of size of 0.1 mm × 0.01 mm located on the left side at y = 0.05 mm, which was created by setting the damage parameter, d = 1.0.

The final crack paths for these three cases with different crystal orientation distributions are shown in Figures 2.8(a)-(c). The impact of the crystal orientation on the crack path is clearly evident, due to the anisotropic behavior included in the model. As shown in Figure 2.8(d), the corresponding stress strain curves also show the influence of the crystal orientations of the grains. Different slopes are captured in the stress strain curves due to the rotated elasticity tensor in each grain.

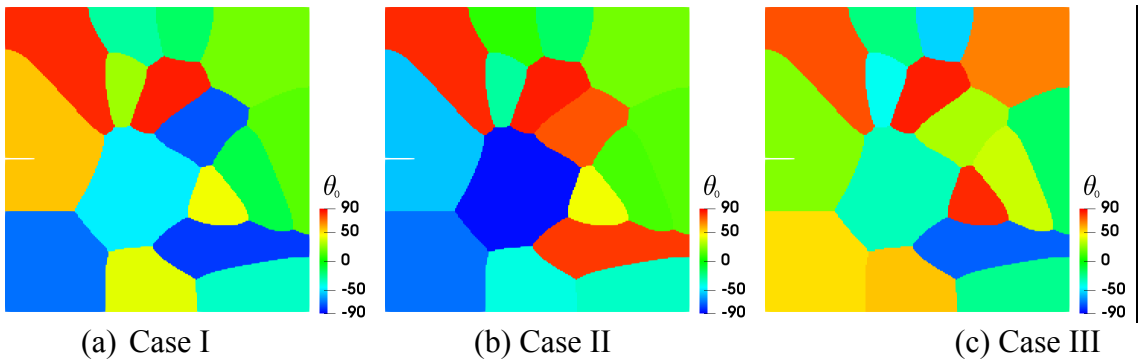

(a) Case I (b) Case II (c) Case III

Figure 2.7. Three cases of crystal orientations performed on the polycrystal structures.

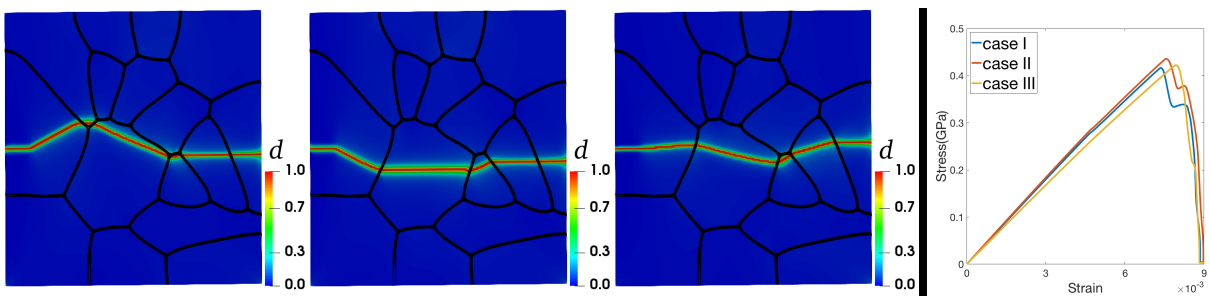

(a) Crack path I (b) Crack path II (c) Crack path III (d) Stress strain curves

Figure 2.8. Final crack paths in the three different polycrystal cases with anisotropic fracture energy, where (a)-(c) shows the corresponding crack paths for the polycrystalline textures shown in Figures 2.7(a)-(c), respectively. The corresponding stress strain curves are shown in (d).

3.4 Application to SiC

In order to obtain the material parameters of SiC, molecular dynamics (MD) simulations have been carried out. Details are provided in section 3 of this report. In the phase field simulations of SiC, fracture in a bicrystal structure is modeled, where the geometry is shown in Figure 2.9a, with the same elastic constants as obtained from MD. Phase field fracture simulations were conducted, and the value g_c was found that gave the closest comparison between the phase field and MD simulation results. The fitted value was $g_c = 1.2\ \mathrm{GPa} \cdot \mathrm{nm}$, as shown in Figure 2.9b.

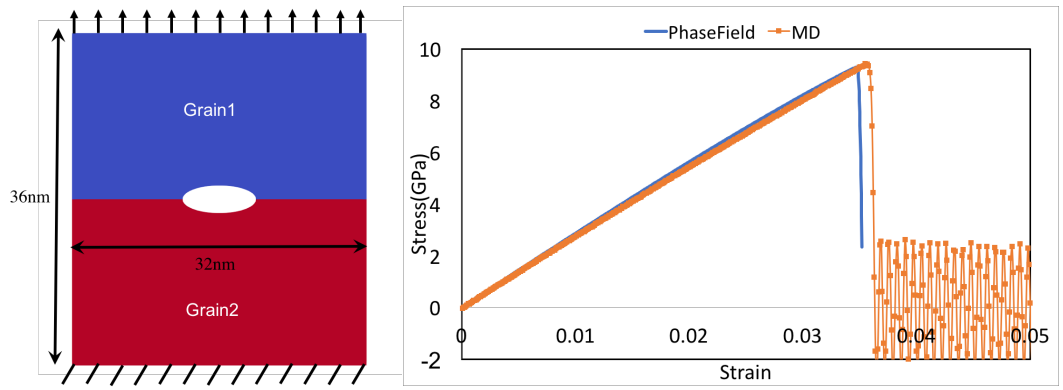

Figure 2.9. Geometry size and stress strain curves obtained by phase field and MD simulations. (Left) Geometry size of bicrystal structure. (Right) Stress strain curves comparison with MD simulations.

Using the fitted value for g_c and the elastic constants from the MD simulation, a 25 grain SiC polycrystal structure of size 10μm×10μm was studied. It has an initial crack length of 3 μm and random crystal orientations, as shown in Figure 2.10(a). The resultant impact on the elasticity tensor $C_{1111}(GPa)$ (labeled as C_{11}) is shown in Figure 2.10(b). The bottom side is fixed, while the top side has an applied displacement rate of 10^{-4}μm/s. The stress distribution and crack path are shown in Figure 2.10(c). The stress distribution shows that the tensile stress drives the crack propagation, and the crack path is transgranular. This simulation assumes isotropic fracture energy; the SiC specific anisotropic fracture energy is still under development.

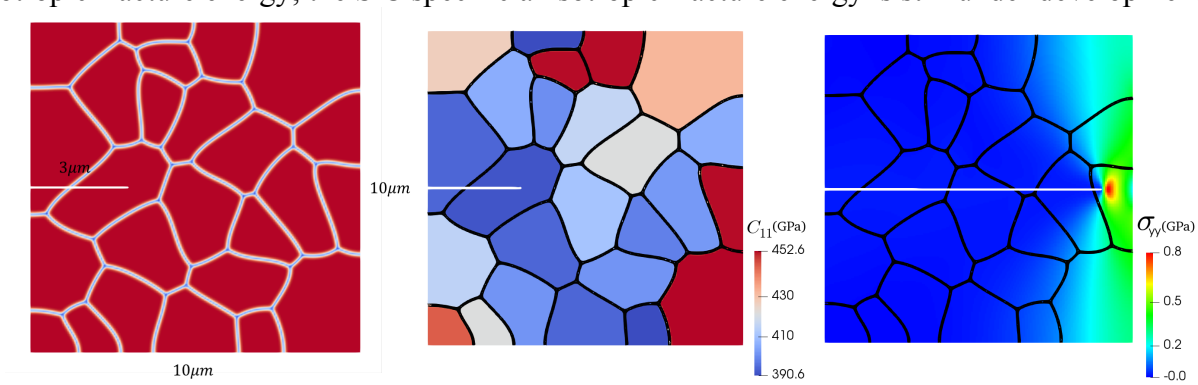

(a) Simulation geometry (b)Crystal orientations resultant C_{1111} (c) Crack path and stress distribution

Figure 2.10. The 25 grain polycrystal structure used for crack simulations, where the geometry size is shown in (a), the crystal orientations performed on the polycrystal structure and its resultant C_{1111} are shown in (b), the final crack path and stress distribution are shown in (c).

4 Traction-separation curves for grain boundary (GB) fracture

We performed molecular dynamics (MD) simulations of fracture of 3C-SiC, using single crystal samples, as well as bicrystals that contain GBs. For single crystals, we choose (100), (110), and (111) plane perpendicular to the direction of applied stress, which is along z direction in Figure 3.1. Coherent GBs with tilt angles smaller than 15° are generated by tilting two crystals. When two grains were attached together, there is an interface created. However, after this procedure there will be some atoms that are positioned too close to each other. We deleted one of the atoms if two atoms are closer than 1.9 Å. In total, three coherent GBs were created by tilting single crystal with a (110) orientation around the y direction (which corresponds to [100]) to angles of 11.3°, 4.4°, and 2.1°. The resulting coherent GBs had coincident site lattices 13, 85 and 365, and are referred to as GB $\Sigma 13$, GB $\Sigma 85$ and GB $\Sigma 365$, respectively. In both single crystal and bi-crystals, the dimensions of the SiC sample are 30 Å, 300 Å, and 360 Å, along the *x, y* and *z* directions, respectively. Similarly to Refs. [2,3], atoms in the center of SiC simulation cells are deleted to initiate the fracture, which results in an elliptical through-thickness void that is 80 Å long and 20 Å high. Each sample was equilibrated at 300K for 2.5 ps, then relaxed at 500K for 5 ps, and finally quenched to 300 K for 5 ps in isothermal-isobaric (NPT) ensemble at zero pressure. The structures of coherent GBs obtained at the end of our equilibration simulations are the same as those previously reported in MD simulations with a different SiC potential [1,4]. They have similar units as GBs in diamond [5] and cubic-Si [6], as determined from MD simulations and validated against electron microscopy images [7]. Using the same optimization procedures, we obtained equilibrated structure of incoherent GBs.

After each sample was equilibrated, we subjected it to a uniform uniaxial strain. The samples are strained at a constant velocity of 10^{-4}/ps along the z direction, which corresponding to a nominal engineering strain rate of 10^{8}/s. The other two directions are free to move to maintain zero stress. Periodic boundary conditions were applied within the GB plane, i.e., along the x and y directions. The simulation temperature was kept at 300 K. The temperature and pressure are controlled using the Nose-Hoover thermostat and barostat [8–10]. All simulations were carried out using the LAMMPS package [11].

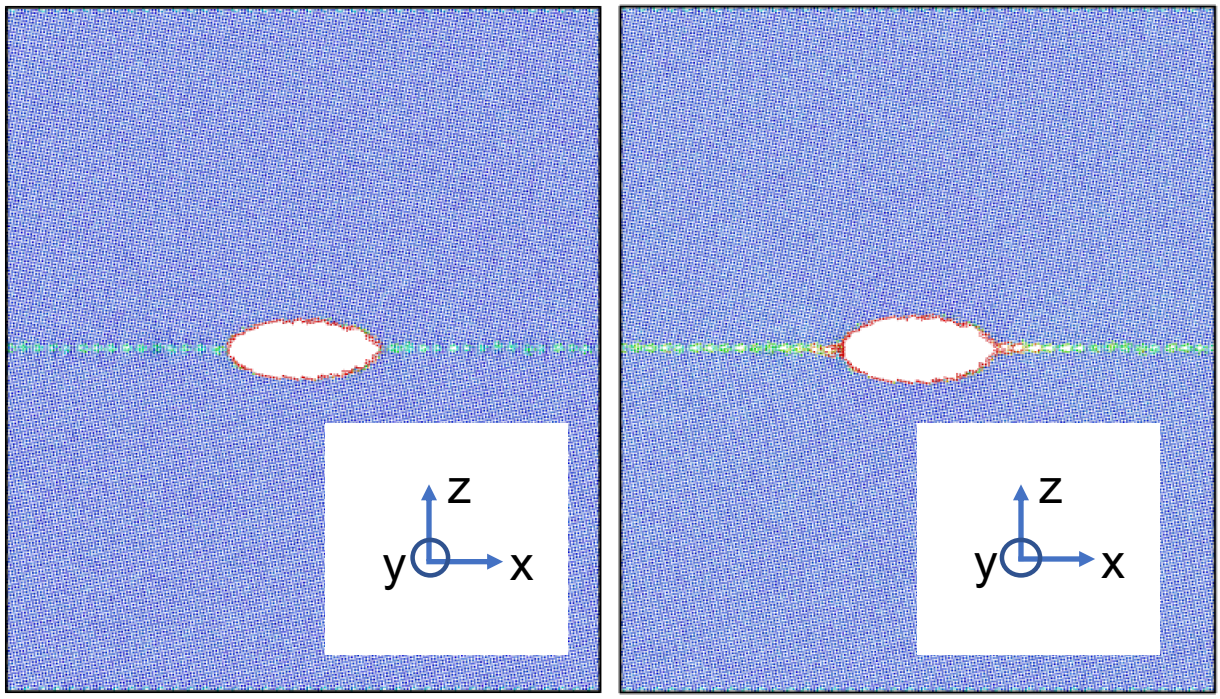

Figure 3.1. Schematic of a simulation cell at 0 (a) and 0.01 (b) strain. GBs and elliptical notches are at the center of each simulation cell. The color code in (a) and (b) is the same, and it shows atomic volume that ranges from 9 $Å^3$ (blue) to 12 $Å^3$ (red).

For bicrystals with GBs, the crack was found to propagate along GBs. As see in Figure 3.2, the stress-strain curve, i.e., the normal stress as a function of normal strain along z direction, is plotted and it displays a feature of brittle failure. For bicrystals with GB Σ13, no plastic deformation was observed at crack tips during crack propagation. Compared with GB Σ85 and GB Σ365, GB Σ13 has a higher tilt angle and more dense dislocation cores along GBs. Once there is a micro-pore nucleated at the initial elliptical notch, the crack propagates along GB quickly and results in a brittle fracture. For bicrystals with GB Σ85, micro-pore nucleated not only at the initial notch but also at dislocation cores along the GB. Nucleation of the multipole voids released some of the stress and made it more difficult to initiate and propagate a single crack. That is the reason why with GB Σ85 has a larger fracture strength. For bicrystals with GB Σ365, as the rotation angle is only 2.1°, at the beginning local stress concentration appears mostly at the elliptical notch instead of dislocation cores. As the strain increases, there stress concentrated at dislocation cores can be released, which is manifested as fluctuations in the stress-strain curve. After the crack has been initiated from the elliptical notch, it quickly propagates along the GB.

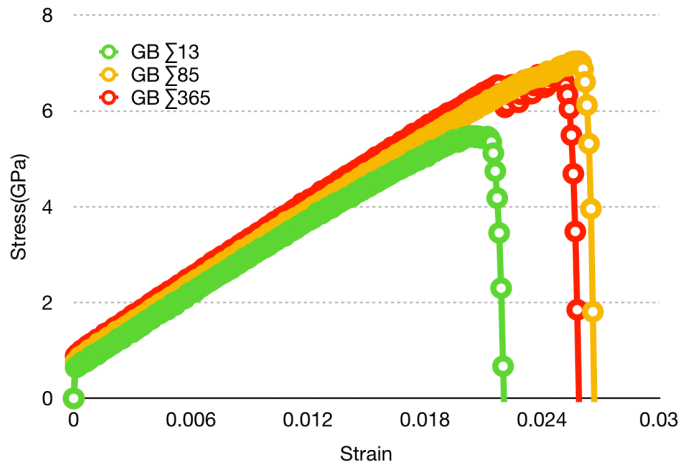

Figure 3.2. Stress-strain curve for bicrystals with GB Σ13, GB Σ85, and Σ365.

For single crystals, we simulated samples with (001), (011) and (111) plane perpendicular to the applied strain. To clarify the effect of GBs in former discussion, we rotate the single crystal with (011) plane perpendicular to stress by 11.3°, 4.4° and 2.1° to create single crystals that have the same structures as the upper half crystals of bi-crystals with GB Σ13, GB Σ85, and Σ365. They are referred as No GB Tilt 11° (Σ13), No GB Tilt 4°(Σ85), and No GB Tilt 2° (Σ365) in the following discussion. The strain-stress curves are plotted in Figure 3.3. They show that, in all single crystals, there is no plastic deformation observed at the crack tips during the crack propagation, which is consistent with the results reported in Ref. [12]. Comparison of Figure 3.2 and Figure 3.3 shows that, as expected, the presence of the GB decreases fracture strength. The trend in fracture strengths persists between single crystals created by rotating (011) plane and bi-crystals with corresponding GBs. For example, the fracture strength and toughness of bicrystals with GB Σ365 is larger than that of bicrystals with GB Σ13 and less than that of bicrystals with Σ85. Similarly, in single crystals, the fracture strength and toughness can be ordered in the sequence of No GB Tilt 11° (Σ13) < No GB Tilt 2° (Σ365), < No GB Tilt 4° (Σ85).

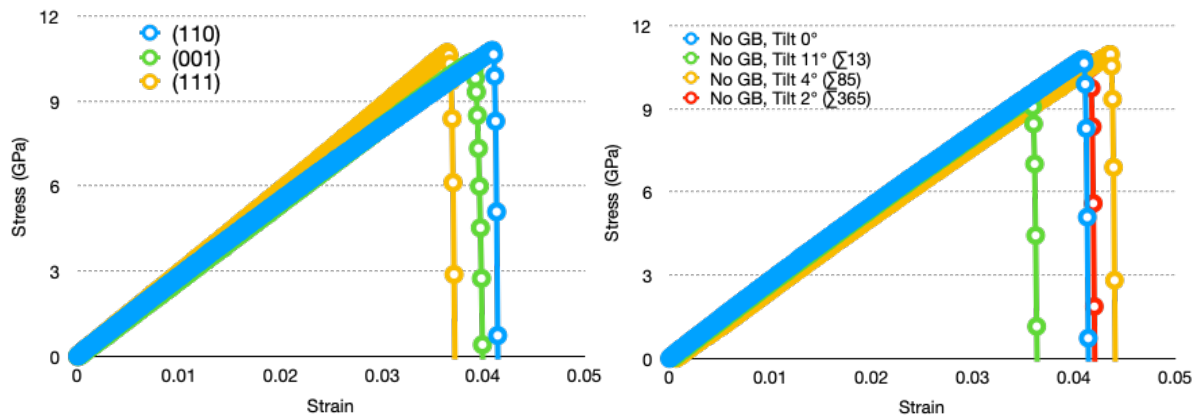

Figure 3.3. Stress-strain curve for single crystals with (001), (110), and (111) plane perpendicular to stress. Single crystals created by rotating single crystal with (110) plane 11.3°, 4.4° and 2.1°, which have the same crystal structures of upper half crystals of bi-crystals with GB $\Sigma 13$, GB $\Sigma 85$, and $\Sigma 365$.

Wang, *et al.*[13] have previously reported that CVD grown SiC can be off-stoichiometric near 3C-SiC GBs. In order to simulate the effect of atom depletion on SiC fracture, we introduced 5% of carbon and silicon vacancies near a GB of bicrystals and near the center plane of single crystals. The corresponding strain-stress curves are shown in Figure 3.4. The results indicate that the presence of vacancies significantly decreases the fracture strength and toughness of single crystal while vacancies have little effect on the fracture of bi-crystals.

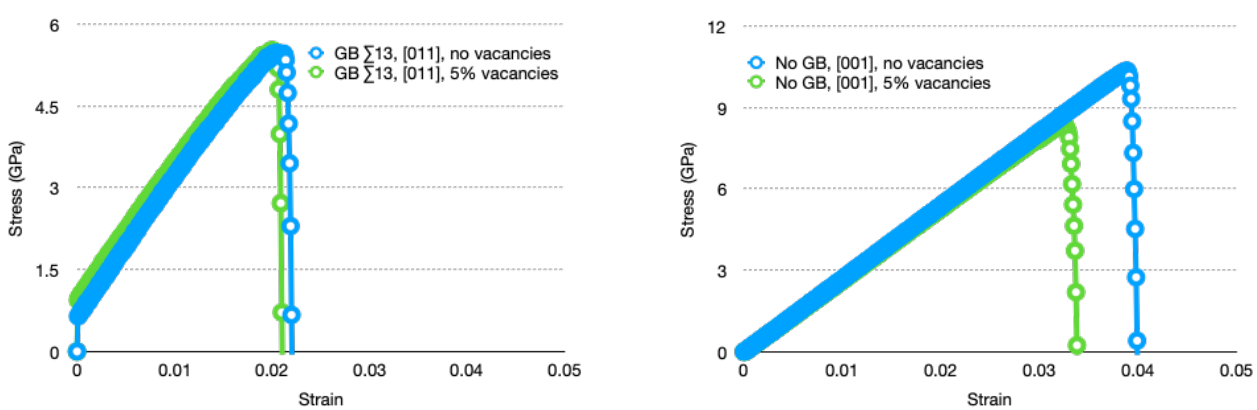

Figure 3.4. (a) Strain-stress curves of bicrystals with GB Σ 13 and bicrystals with 5% vacancies near GB. (b) Strain-stress curves of single crystal with (100) plane perpendicular to stress and same single crystal with 5% vacancies near middle plane.

5 Prediction of radiation-induced swelling

Distribution of black spot defects (BSDs) and small clusters in irradiated 3C-SiC has been investigated by combining microscopy characterization with cluster dynamics (CD) model. It is found that there are small clusters identified in scanning transmission electron microscopy (STEM) invisible in TEM images. Simulations showed that both established properties of point defects (PDs) generation, reaction, clustering, and cluster dissociation, and additional phenomena of clusters generation, diffusion and morphology preference are necessary to be considered in a predictive model on cluster evolution in ion irradiated SiC. In this project, based on CD formalism, we developed a swelling model to estimate the swelling contributed by defects, which qualitatively explains that the swelling estimated based on X-Ray diffraction (XRD) is larger than that based on TEM is because there are PDs and small clusters invisible from TEM.

Many studies via conventional TEM have been dedicated to understanding distributions of defects in this regime and their contributions to swelling and creep [14,15]. For instance, Katoh *et al.* [14] used TEM to measure the distribution of defect clusters in irradiated SiC and used this information to estimate the expected swelling. Interestingly, only 10–45% of the macroscopically measured swelling was accounted for by the clusters and loops that were visible in TEM. One of the outstanding challenges in this field is to be able to measure and quantify a distribution of very small defect clusters that are difficult to measure in traditional TEM. These defects are often referred to as BSDs because of their appearance in TEM bright field images, if they are visible at all. These defects are often assumed to be small interstitial clusters because in this temperature range vacancies are immobile [16] (migration barriers for Si and C vacancies are 2.4 and 3.67 eV, respectively [17]) and therefore vacancies can hardly form extended defect clusters.

We have developed a CD model of cluster evolution in irradiated SiC to determine the amount of swelling and the predictions were compared to experimental measurements. The number of point defects (PDs) present in irradiated samples can be estimated as follows. As both carbon and silicon interstitials diffuse very fast and have a strong tendency to cluster, there are few isolated interstitials left in matrix. On the other hand, once an interstitial is trapped in a cluster, it is difficult for this interstitial to be emitted or react with isolated vacancies or antisites (since the latter two defects have relatively high migration barriers and do no diffuse easily[17]). In our CD model the ratios between the number of interstitials trapped in clusters and the number of isolated interstitials, vacancies, and antisites reach approximately constant values as the simulation progresses. The CD model, which is optimized to reproduce clusters size distribution for clusters with diameters $D < 2.5$ nm, can be used to determine the number of isolated interstitials, vacancies, and antisites. The number of interstitials trapped in clusters with $D < 2.5$ nm can be calculated based on the experimental cluster size distribution by multiplying the estimated cluster area by the Burgers vector, and then dividing by the atomic volume of 3C-SiC. The ratios of interstitials trapped in clusters over isolated interstitials, vacancies, and antisites calculated using this method are listed in Table 4.1. We then calculate the total number of interstitials trapped as clusters and in this calculation we count clusters of all sizes observed in

TEM and STEM, including those with $D > 2.5$ nm. The total number of trapped interstitials is then multiplied by the ratios from Table 4.1 to obtain the total number of isolated points defects that are present in the samples (it is not possible to observe these PDs directly in TEM).

Table 4.1. *Ratio between the number of isolated PDs and the number of interstitials trapped in clusters, as well as formation volumes of defects. Formation volumes are taken from Ref.[18] the method to calculate the ratios is explained in text.*

	C_I	Si_I	V_C	V_{Si}	C_{Si}	Si_C
Ratio of isolated PD to cluster-trapped interstitials	0.258×10^{-8}	0.110×10^{-9}	0.599	0.246	0.240	0.414
Formation Volume (Å^3)	15.33	37.22	2.68	1.85	-9.52	15.44

Swelling caused by the presence of clusters can be calculated by multiplying their areas by their Burgers vector. Contributions to swelling from isolated PDs can be derived by multiplying their concentrations by their formation volumes, which have been determined in Ref. [18] and are reported in Table 4.1. Using the above approach, the total swelling is calculated to be 0.155% in our sample, which was irradiated with 1 MeV Kr^+ at temperature 1073 K to a fluence of 3×10^{14} Kr/cm^2. This swelling was measured at the location in the sample that corresponds to the dpa of 0.24. Our estimated swelling is on the same magnitudes the results of Price *et al.* [19], who irradiated 3C-SiC at 1053 K with fast neutrons (E > 0.18 MeV) to 6×10^{21} n/cm^2, and the measured the swelling was 0.4±0.1%.

As shown in Figure 4.1, using our swelling model we find that 38.13% of the total swelling comes from isolated PDs, 10.77% of the total swelling comes from BSDs or smaller clusters ($D < 1.0$ nm) where TEM underestimates the cluster concentration, and 51.10% of the total swelling is caused by larger clusters or dislocation loops ($D > 1.0$ nm). This analysis is consistent with the observation that volume expansion calculated based on the concentration of defects loops visible in traditional TEM accounts only for one third of the total swelling in SiC [15]. The mismatch between TEM based calculation and measured swelling is largely due to the small BSDs and isolated PDs that cannot be easily characterized by TEM. In addition, from the 38.13% of swelling that is due to PDs, interstitials contribute only less than 0.01% of swelling (most of the interstitials are found in clusters), while vacancy and antisites contribute 33.35% and 66.65%, respectively.

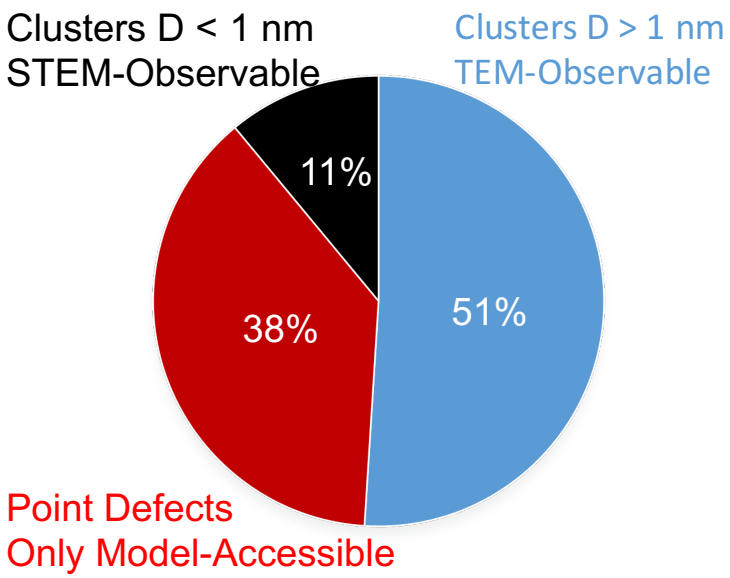

Figure 4.1. Relative contribution to total swelling estimated from PDs, clusters with diameter smaller than 1 nm and clusters observable from TEM (D > 1 nm).

To further validate our swelling model, high resolution TEM was employed to study the size distribution of BSDs in ion-irradiated 4H-SiC. Swelling estimations based on swelling model developed above and TEM data were compared to swelling measured indirectly via X-ray diffraction. To simulate neutron irradiation, 4H-SiC was irradiated by 3.15 MeV C^{2+} and 1 MeV Kr^{+} at 600°C, 800°C, and 950°C up to 0.4 DPA and 0.8 DPA. DPA values were calculated at the depth of 1 µm, see Figure 4.2, assuming the threshold displacement energies of 20 eV and 35 eV for C and Si, respectively.

TEM imaging was conducted on a FEI Tecnai TF30 TEM operated at 300 keV. The ion-irradiated 4H-SiC were examined along a $[11\bar{2}0]$ zone axis in areas typically within 200 nm and 1500 nm from the irradiated surface for krypton- and carbon-irradiated SiC. For each sample, the depth of the TEM observation is compared to SRIM calculations to determine the true DPA or the observed sample area. The thickness of each observed area was determined using the log-thickness method applied to low-loss EELS spectra and an inelastic mean free path of 165.65 nm.

BSDs appear as nanoscale black regions in bright-field TEM images. Identifying BSDs using a global intensity threshold for the entire image has limited accuracy due to background contrast variability, presumably from strain, in the ion irradiated sample. Therefore, we adopted a method that identifies BSDs using local intensity thresholds, which compare BSDs only to their immediate environment. The method was implemented in MATLAB.

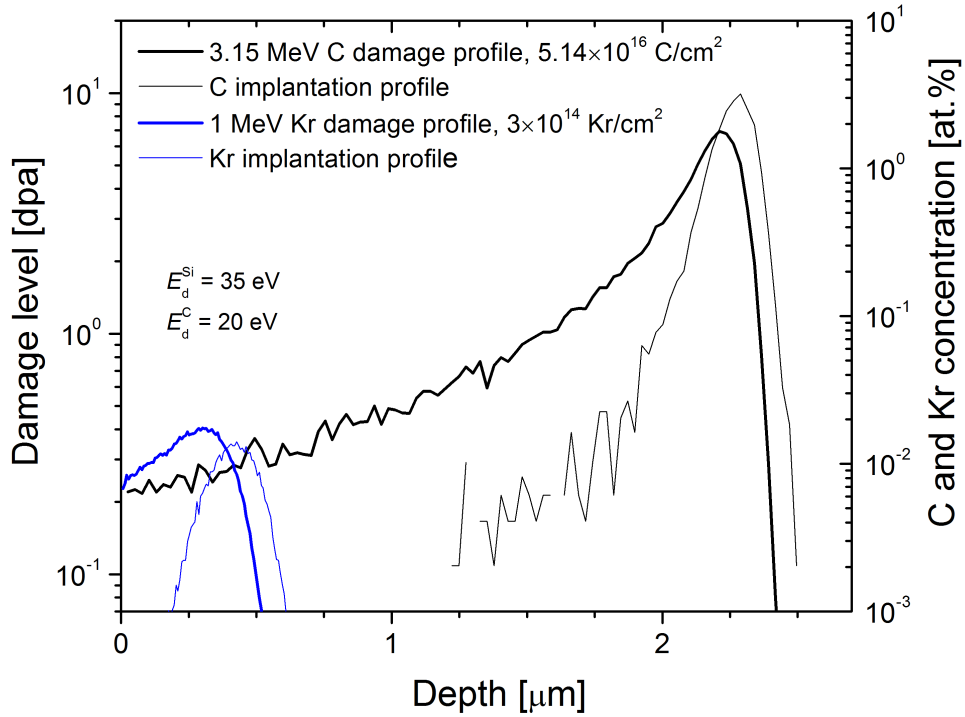

Figure 4.2. Damage and C and Kr ion distributions in SiC irradiated with 3.15 MeV C and 1 MeV Kr ions to a damage level of 0.4 dpa at the depth of 1 μm and peak, respectively. Calculations were performed using SRIM-2012.03[20] assuming the displacement threshold energies to be 20 eV for C and 35 eV for Si.

Swelling is calculated based on defect size distribution determined in TEM. Total swelling in this report is then estimated by adding formation volumes of all the defects present in the system (including clusters and isolated point defects). The calculated swelling is shown in Table 4.2, swellings calculated from based on TEM are on the same order of magnitude with those calculated based on XRD, however in many cases TEM underestimated XRD by a factor 10%-80%. The likely reason for this discrepancy is that there are probably smaller clusters present in SiC, however they are invisible to TEM. Such clusters have been reported based on observations from high resolution STEM. The conclusion that TEM underestimates cluster size concentration for small clusters is consistent with previous results by Katoh *et al.*[21], who reported neutron irradiation of SiC at 800 ℃ up to $4.5\times10^{25}\ n/m^2$. In their study the total estimated swelling from the loops was an order magnitude smaller than swelling estimated from XRD. The smaller discrepancy in our results between swelling estimated from TEM and XRD (Table 4.2) than in the study of Katoh *et al*'s is due to the fact that we accounted for contributions to swelling from isolated point defects, in addition to the contribution from clusters. We find that contribution from all point defects constitutes 38% of the total swelling calculated based on TEM and therefore it is important to include this contribution.

Another possible source of discrepancy between XRD and TEM analysis of swelling is that XRD data is averaged over a thicker specimen (bulk measurement) than typical TEM samples (0.2 µm). Since in ion implantation, there is a depth dependence of the damage profile, corrections for such damage distribution should be introduced to TEM based analysis in order to predict the overall swelling of the sample. Such correction would require a detailed knowledge of the relation between local DPA and the defect size distribution, which is beyond the scope of this thesis.

Table 4.2 Summary of the swelling results from XRD and TEM for the single crystalline 4H-SiC implanted by 3.15 MeV C up to 0.4 DPA and 1 MeV Kr up to 0.4 and 0.8 DPA at various temperatures. Swelling from XRD (at the nominal damage level) was calculated using strain values at the peak maximum indicated in the brackets. Swelling from TEM was based on BSD size and density data.

Irradiation conditions		Swelling XRD [%] (nominal DPA)	Swelling TEM [%] (actual DPA)	Swelling model & TEM [%] (actual DPA)
3.15 MeV C	600 °C	0.580 (0.4)	0.318	0.623 ± 0.094 (0.37)
	800 °C	0.466 (0.4)	0.116	0.228 ± 0.042 (0.34)
	950 °C	0.381 (0.4)	0.114	0.223 ± 0.032 (0.32)
1 MeV Kr	600 °C	0.741 (0.4)	0.09	0.176 ± 0.025 (0.21)
	600 °C	0.750 (0.8)	0.115	0.225 ± 0.035 (0.57)
	800 °C	0.472 (0.4)	0.073	0.144 ± 0.022 (0.24)
	800 °C	0.482 (0.8)	0.291	0.570 ± 0.089 (0.62)

A swelling model has been developed based on the CD technique. It provides an explanation for the discrepancy between swelling measured experimentally and swelling estimated based on dislocation loops observed in traditional TEM examination. This discrepancy is due to the presence of very small clusters and isolated PDs, which both have a non-negligible contribution to the total swelling.

6 Mechanical properties of unirradiated and irradiated SiC

6.1 Sample fabrication and experimental methods

As-synthesized 3C-SiC bulk samples were made by chemical vapor deposition and were polished before TEM sample preparation. Bulk 3C-SiC samples were irradiated with carbon ions with 5.15 MeV energy under different temperatures and fluences, as shown in Table 5.1. Standard TEM samples of as-synthesized SiC, 600 °C 3 dpa and 600 °C 0.3 dpa were fabricated using focused ion beam (FIB, Zeiss Auriga) with 5 keV / 100 pA as the last milling step to a final sample thickness of around 80 nm. Standard samples were observed in TEM (Tecnai TF-30, 300 keV) to characterize the microstructure before indentation. Samples for *in situ*

indentation tests started with pieces about 1.5 μm thickness (15 μm x 7 μm), lifted out from the bulk material using an Omniprobe micromanipulator in the FIB. The pieces were welded on Si wedge-shaped substrates (Hysitron Si wedge, 1 μm plateau) and thinned down to ~150 nm with 5 keV / 100 pA as the last milling in FIB. Ar ion nanomilling at 900 eV (Fischione 1040 Nanomill) was used to do the last polishing before indentation in order to reduce amorphous layer created by Ga ion damage. *In situ* indentation tests were performed in TEM (Tecnai TF-30, 300 keV) with a single tilt PicoIndenter holder (Hysitron PI 95 PicoIndenter) operated in displacement control mode with velocity 10 nm/s. Force-displacement curves and videos of indentation were obtained simultaneously. Characterization after indentation tests was done in TEM (Tecnai TF-30, 300 keV) and scanning electron microscopy (SEM, Zeiss/LEO 1530).

Table 5.1. 3C SiC irradiation conditions.

	300°C	600°C	900°C
[/cm^2] dpa		[1.5×10^{16}] 0.06	
[/cm^2] dpa		[7.5×10^{16}] 0.3	
[/cm^2] dpa	[1.5×10^{17}] 0.6	[1.5×10^{17}] 0.6	[1.5×10^{17}] 0.6
[/cm^2] dpa		[7.5×10^{17}] 3	

6.2 *In situ* nanoindentation studies on as-synthesized 3C-SiC

3C-SiC is a brittle material in bulk, but our *in situ* nanoindentation tests observe some room-temperature plasticity at the nanoscale. The typical phenomenon we observed *in situ* is the generation and movement of sets of dark contours in bright-field TEM, as is shown in Figure 5.1A. These features are bend contours, which are electron diffraction phenomena arising from changes in the local orientation of the crystal with respect to the electron beam [12]. In this case, they primarily indicate that the sample is bending during indentation. However, previous experimental results and simulations have shown that bend contours provide insight into sample mechanical properties by

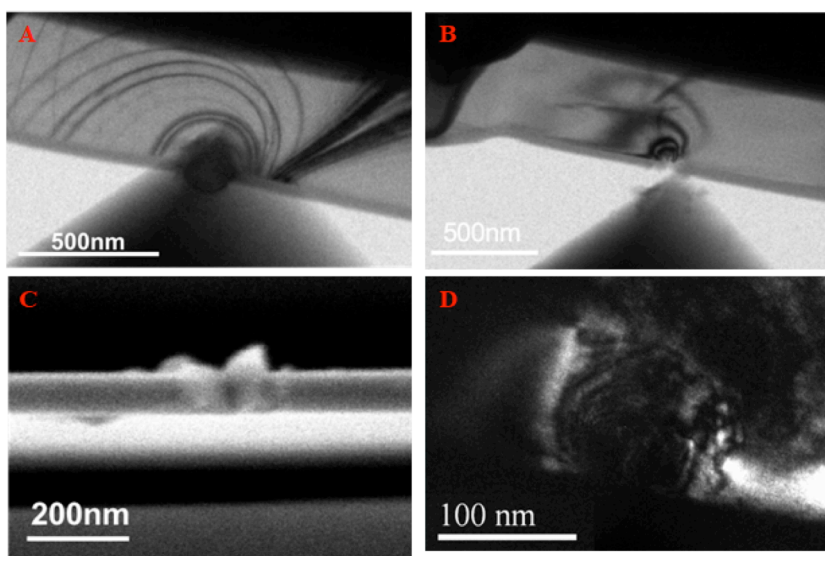

Figure 5.1: In situ indentation of unirradiated 3C-SiC. (A) Bend contours during indentation in BF TEM. (B) Bend and a residual indent post indentation in BF TEM. (C) A side view of the extrusion from the sides of the indent in the SEM. (D) Post-indent DF TEM showing residual bend contours.

representing strain fields in fairly a straightforward way [13-15]. In particular, the bend contours are not fully reversible in the *in situ* test. The field of view for Figure 5.1A was free of contours before indentation, but in Figure 5.1B, after indentation, some of the contours remains.

Figure 5.1B also shows the imprint left on the sample after the indenter was removed. Figure 5.1C is a side view of the same indent, acquired in the SEM after testing. Both Figure 5.1B and 5.1C show a metal-like extrusion around the imprint. Figure 5.1D is close-up dark-field TEM image post indentation showing localized bend contours surrounding the indent. The extrusion and retained bend contours indicate that the sample underwent some plastic deformation during indentation and that it retains some plastic strain after the test is completed. Room-temperature plasticity of SiC derived from amorphization [14], phase transformation [16], and glide of dislocations [17], have been reported in the literature. Since plastic deformation in our thin 3C-SiC compression tests is quite similar to the conventional plastic deformation in metals, which is usually associated with the generation and propagation of dislocations, we speculate that the room-temperature plasticity in thin 3C-SiC may have a similar mechanism.

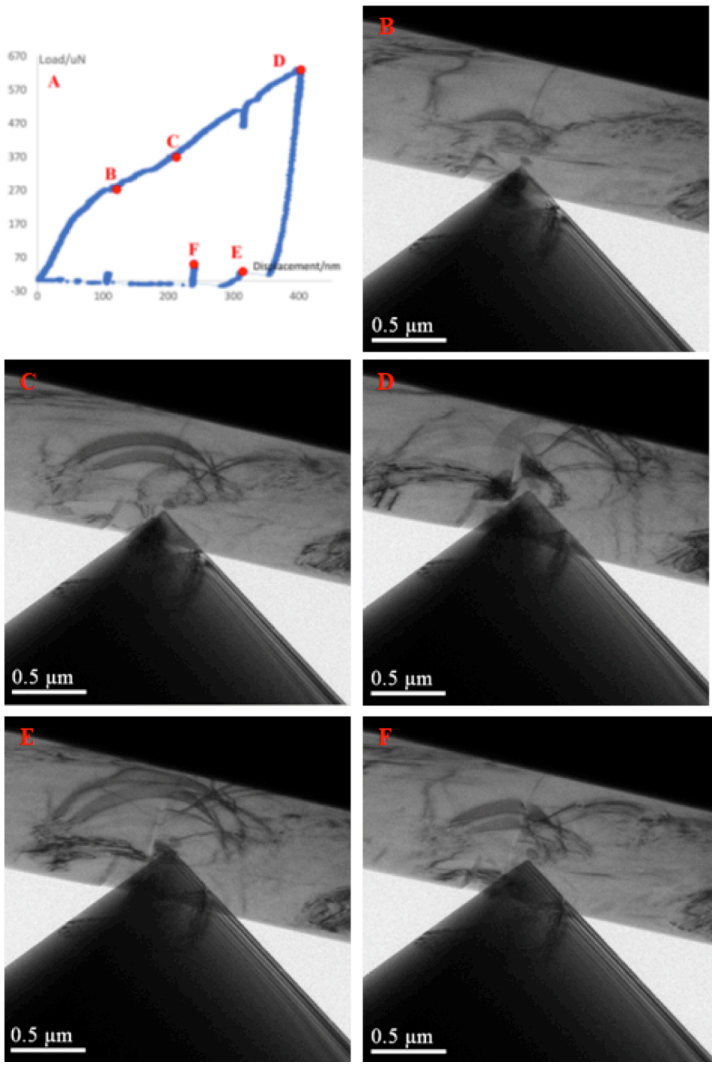

Figure 5.2 (A) Load-displacement curve of nanoindentation test on as-synthesized 3C-SiC and (B) – (F) images of the microstructure at the points indicated the curve in (A).

The biggest advantage of *in situ* nanoindentation is acquiring the video of microstructure evolution and the load-displacement curve simultaneously. Comparing these data can identify specific changes of with the corresponding mechanical behavior. Figure 5.2A is the load-displacement curve from one indentation test on an as-synthesized 3C-SiC sample and Figure 5.2B-F are images extracted from *in situ* video at the position marked in A. Figures 5.2B and

5.2C are during loading, when the contours are generated and moving and both elastic and plastic deformation are happening. In Figure 5.2A, at the point D, the force drops dramatically, corresponding to the elastic deformation recovery on unloading. Starting from point E, the force reaches zero, then fluctuates. However, in Figures 5.2E & 5.2F, contours are still moving backward to the surface. Thus, it is possible that the sample has partial plastic deformation recovery. The tail shown in the force-displacement curves between D and E points from *in situ* nanoindentation test is similar to the tail shown in the stress-strain curve of nanocrystalline Al sample undergoing plastic deformation recovery in a large scale molecular dynamic simulation [18]. We believe the back stress necessary for plastic deformation recovery could be provided either by free surfaces or the thicker region of the sample visible as the black region I the upper right corner of the images in Figure 5.2 [19].

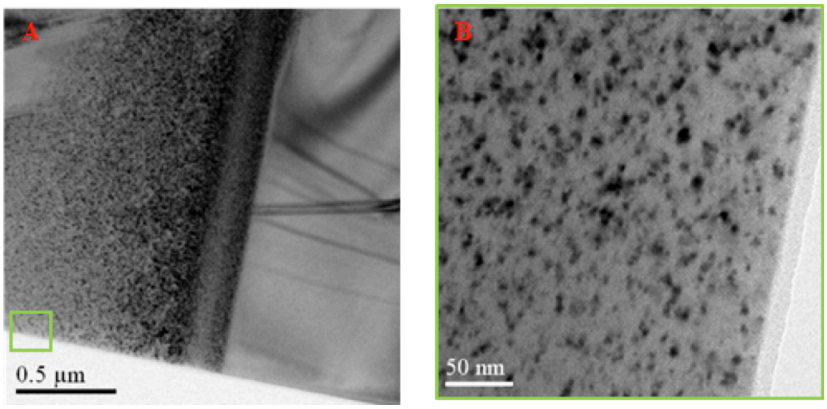

Figure 5.3 Bright-field TEM images of the 600 °C, 3 dpa sample. (A) Low-magnification image. Ions enter the sample from the right, so the end of range is visible. of small defects caused by irradiation. (B) Higher magnification image inside the green box in (A) showing small defect clusters.

6.3 In situ nanoindentation studies on irradiated 3C-SiC

3C-SiC exhibits various microstructures under different radiation conditions. Under relatively low dose and low temperature, black spot defects and point defects and/or their clusters are the main defects. As the temperature increases or radiation dose increases, defects are mostly Frank loops, dislocation networks or even voids [20]. We have characterized the microstructure of the 3C-SiC samples irradiated under the conditions in Table 5.1. Figure 5.3A shows the defect distributions along the implantation profile, with a maximum defect density near the 3.5 μm depth calculated by SRIM. Figure 5.3B is the higher magnification bright-field TEM image inside the green square in Figure 5.3A, in which most of the defects are small defects and/or their clusters with size smaller than 10 nm.

In situ nanoindentation tests on irradiated 3C-SiC were done on two irradiation conditions, 600 °C 3 dpa and 600 °C 0.3 dpa, with several TEM samples and multiple tests per sample. Indentation tests on 600 °C 3 dpa samples, such as Figure 5.4A, suggest that elastic deformation happens similarly to as-synthesized samples, but then fracture is likely to happen with long, clear and simple crack path, as shown in Figure 5.4B. This kind of single, straight crack was observed in 86% of tested samples on irradiated areas. The lengths of cracks are from 550 nm to 800 nm. The remaining samples either did not fracture within the load and displacement limits of the test, or (rarely) fractured with a branching crack. For 600 °C, 0.3 dpa samples, indentation tests indicate similar deformation behavior as 600 °C 3 dpa samples, fracturing with a single, straight crack as shown in Figures 5.5A and 5.5B. Compared to the higher dpa sample, the cracks are shorter, with ~400 nm being typical, and not as sharp.

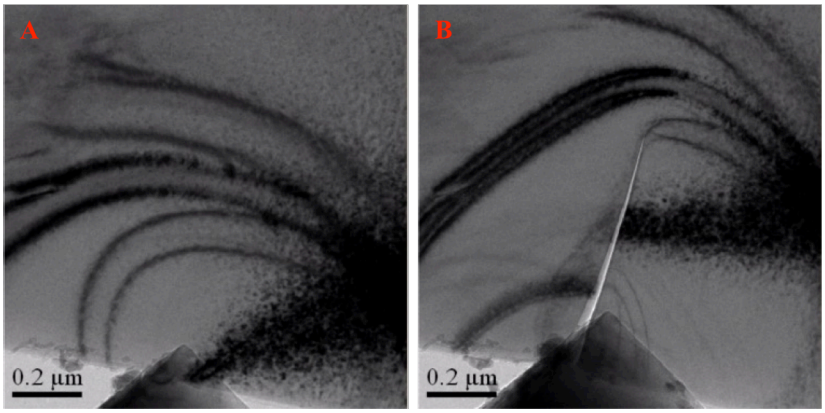

Figure 5.4 Images (A) before and (B) after fracture of the 600 °C, 3 dpa sample.

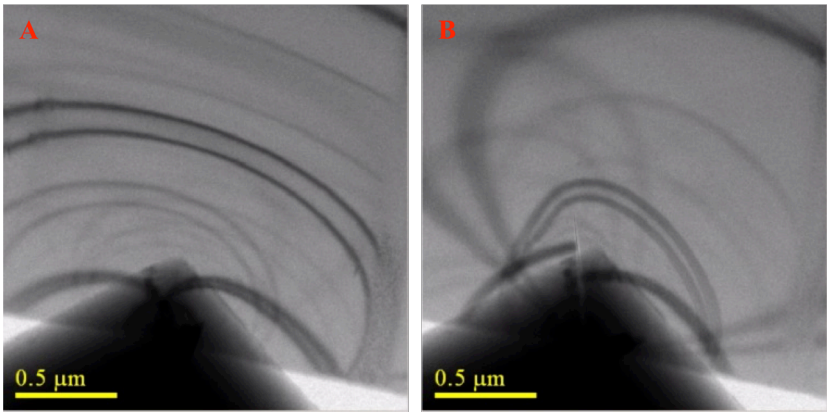

Figure 5.5 Images (A) before and (B) after fracture of 600 °C, 0.3 dpa SiC sample.

This behavior is in stark contrast to fracture of the unirradited samples. When those samples fracture, it is with a complicated, branching set of micro-cracks, leaving behind a distinct indent and a significant amount of debris, as shown in Figures 5.1B and 5.1D. We therefore conclude that irradiated 3C-SiC is embrittled and has lower fracture toughness than as-synthesized 3C-SiC. This is supported by the longer, straighter cracks that occur with higher dpa at 600 °C. This behavior is in contrast to results from microindentation tests on bulk irradiated 3C-SiC, which show shorter and more complex cracks in irradiated SiC, consistent with higher fracture toughness [21]. This difference may arise because of differences in irradiation

conditions or differences in sample size and geometry and the reasons are still being investigated.

6.4 *Ex situ* nanoindentation studies

3C-SiC bulk samples irradiated the conditions in Table 5.1 were polished on a surface perpendicular to the irradiated surface, then subjected to *ex situ* nanoindentation testing (Hysitron PI 980 TriboIndenter). Both the irradiated and unirradiated sides of the sample were tested, and we present the percentage change in properties from the two tests. This approach reduces the influence of substrate effects on the results [22] and makes changes of properties more reliable. We estimate that the uncertainty in the measured hardness and modulus are both ±5%, dominated by the uncertainty in determining the indent area. The results did not vary along the indentation profile in from the irradiated surface, suggesting that the spatial resolution of the nanoindenter was insufficient to observe variation in properties with dpa along the profile. The results presented here are averaged over 0.5 - 2.5 um radiation damage depth. Change of modulus and hardness of irradiated samples are shown in Figure 5.6. Due to is significant, as in previous similar studies [20], but the general trend is that modulus decreases and hardness increases on irradiation.

The fracture toughness, K_C, can be estimated from indentation data using

$$K_c = A\left(\frac{E}{H}\right)^{\frac{1}{2}} \frac{P}{C^{3/2}},$$

where A is a constant, E is modulus, H is hardness, P is maximum load and c is crack length. Because the geometry in the *in situ* tests is not well-controlled, we cannot use the measured

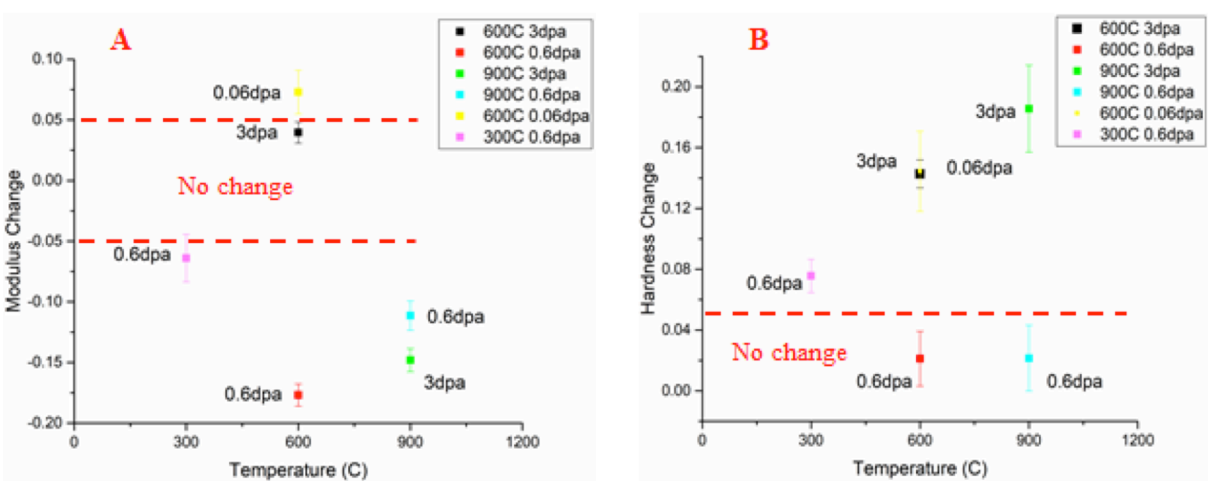

Figure 5.6 Change of modulus and hardness under different radiation conditions

crack lengths to calculate the fracture toughness. However, decreased modulus, increased

hardness, and increased crack length as observed in the combined *in situ* and *ex situ* tests leads qualitatively to decreased fracture toughness.

7 Summary

We have developed a phase field fracture model that predicts microcrack initiation and growth in polycrystalline SiC. The model accounts for single crystal anisotropy, including anisotropy in the elastic constants and anisotropic surface energy. It also considers the reduced fracture strength of grain boundaries. The model was implemented using the MARMOT mesoscale nuclear materials tool. We have parameterized the model for SiC using molecular dynamics simulation results. The model has been verified using single crystal, bicrystal, and polycrystal examples.

Swelling model has been developed based on cluster dynamics simulations of defect evolution in SiC. We found that point defects and small defect clusters have a significant contribution to swelling. This finding is important because point defects and very small defect clusters are not visible in experiments (e.g., in TEM). Combined modeling and experiments can bring critical insights into how swelling depends on irradiation conditions and the microstructure.

In situ nanoindentation tests and *ex situ* nanoindentation tests were performed on as-synthesized 3C-SiC and 3C-SiC irradiated under different radiation conditions. Without radiation, bend contour movement and residual bend contours after indentation demonstrate some room-temperature plastic flow and residual plastic deformation. Plastic deformation recovery is also observed on unirradiated samples during unloading. Radiation-induced embrittlement is demonstrated by differences in crack geometry in *in situ* tests, and is consistent with *ex situ* test results. Failure by single, straight, cracks indicates decreased fracture toughness due to irradiation in 3C-SiC.

8 Conference presentations

1. Xuying Liu, Cheng Liu, Chaiyapat Tangpatjaroen, Izabela Szlufarska, Paul M. Voyles, *"In situ Transmission Electron Microscopy of Room-Temperature Plastic Deformation and Recovery in Thin 3C-SiC"*, Microscopy & Microanalysis Conference, Baltimore, MD, August 2018.
2. Xuying Liu, Chaiyapat Tangpatjaroen, Cheng Liu, Izabela Szlufarska, Paul M. Voyles, *"Irradiation Induced Embrittlement in Thin 3C-SiC Investigated by in situ Nanoindentation via TEM"*, Materials Research Society Conference, Phoenix, AZ, April 2019.
3. C. Liu, I. Szlufarska, "*Evolution of Small Defect Clusters in Ion-irradiated 3C-SiC: Combined Cluster Dynamics Modeling and Experimental Study*", Materials Science and Technology 2017 Annual Meeting & Exhibition, Pittsburgh, PA, October, 2017
4. C. Liu, I. Szlufarska, "*Evolution of Black Spots Defects and Small Clusters in Irradiated 3C-SiC*", 144 TMS Annual Meeting & Exhibition, Orland, FL, Feb, 2015

5. Shuaifang Zhang, Cheng Liu, Izabela Szlufarska, Michael Tonks, *"A Phase Field Model for Simulation of Crack Propagation in Anisotropic Materials and Its Application to Predict Fracture Behavior in Silicon Carbide*", 2018 WCCM, New York.
6. Shuaifang Zhang, Wen Jiang, Cheng Liu, Izabela Szlufarka, Michael Tonks, *"Microstructure-sensitive Phase Field Fracture Model including Anisotropic Elastic Properties"*, 2018 TMS Annual Meeting and Exhibition
7. Michael Tonks, Shuaifang Zhang, Srujan Rokkam, Pritam Chakraborty. *"Predicting the Impact of Material Microstructure on Brittle Fracture Using a Phase Field Fracture Model"*. Materials Science and Technology 2017
8. Shuaifang Zhang, Cheng Liu, Izabela Szlufarska, Michael Tonks, *"Multi-scale Modeling of Fracture Behavior in SiC with a Phase Field Fracture Model"*, 2017 TMS Annual Meeting and Exhibition
9. Shuaifang Zhang, Wen Jiang, Dung-Uk Kim, Michael Tonks, *"A Phase Field Model of Crack Propagation in Anisotropic Brittle Materials"*, Semi-finalist presentation for the Melosh Medal competition, Raleigh, NC, April 26, 2019
10. Tonks, M.R., Zhang, S.G, Chakraborty, Rokkam, S., *"Predicting the Impact of Material Microstructure on Brittle Fracture Using a Phase Field Fracture Model"*, Materials Science and Technology (MS&T 17), Pittsburgh, PA, Oct 8, 2017.
11. **(Invited)** Zhang, S.G, and Tonks, M.R. *" Development of a phase field model to predict the impact of microstructure on brittle fracture with anisotropic elastic constants*", SIAM 2018
12. **(Invited)** I. Szlufarska, C. Liu, D. Morgan, *Computational modeling of materials properties under irradiation,* CERN, Geneva, Switzerland, RaDIATE collaboration meeting, December 2018
13. **(Invited)**, *Computational modeling of materials properties under irradiation*, Fermi National Accelerator Laboratory, Batavia, IL November 2018

9 Publications

1. B. Tyburska-Püschel, Y. Zhai, L. He, C. Liu, A. Boulle, P.M. Voyles, I. Szlufarska, K. Sridharan, *"Size distribution of black spot defects and their contribution to swelling in irradiated SiC*", ***J. Nucl. Mater.*** 476 (2016) 132–139.
2. Shuaifang Zhang, Wen Jiang, Michael Tonks *"A new phase field fracture model in brittle materials including anisotropic elasticity*" ***Computer Methods in Applied Mechanics and Engineering*** (Submitted)
3. Shuaifang Zhang, Wen Jiang, Dung-Uk Kim, Michael Tonks. *"A phase field model of crack propagation in brittle anisotropic materials to predict crack paths*" To be submitted.

4. Xuying Liu , Chaiyapat Tangpatjaroen, Cheng Liu, Izabela Szlufarska, Paul M. Voyles. *"In situ Transmission Electron Microscopy of Room-temperature Plastic Deformation and Recovery in Thin 3C-SiC"* (in preparation).
5. Xuying Liu, Chaiyapat Tangpatjaroen, Cheng Liu, Izabela Szlufarska, Paul M. Voyles. *"Irradiation Induced Embrittlement in 3C-SiC Investigated by in situ and ex situ nanoindentation"* (in preparation).

10 References

1. Katoh, Y., et al., *Radiation effects in SiC for nuclear structural applications.* Current Opinion in Solid State and Materials Science, 2012. **16**(3): p. 143-152.
2. Mecholsky, J. and S. Powell, *Fractography of ceramic and metal failures: a symposium*. Vol. 827. 1984: ASTM International.
3. Katoh, Y., et al., *Current status and critical issues for development of SiC composites for fusion applications.* Journal of Nuclear Materials, 2007. **367**: p. 659-671.
4. Koyanagi, T., et al., *SiC/SiC cladding materials properties handbook.* 2017.
5. Katoh, Y. and L.L. Snead. *Mechanical properties of cubic silicon carbide after neutron irradiation at elevated temperatures*. in *Effects of Radiation on Materials: 22nd Symposium*. 2006: ASTM International.
6. Bourdin, B., G.A. Francfort, and J.-J. Marigo, *The variational approach to fracture.* Journal of elasticity, 2008. **91**(1-3): p. 5-148.
7. Bourdin, B., G.A. Francfort, and J.-J. Marigo, *Numerical experiments in revisited brittle fracture.* Journal of the Mechanics and Physics of Solids, 2000. **48**(4): p. 797-826.
8. Amor, H., J.-J. Marigo, and C. Maurini, *Regularized formulation of the variational brittle fracture with unilateral contact: Numerical experiments.* Journal of the Mechanics and Physics of Solids, 2009. **57**(8): p. 1209-1229.
9. Miehe, C., F. Welschinger, and M. Hofacker, *Thermodynamically consistent phase‐field models of fracture: Variational principles and multi‐field FE implementations.* International Journal for Numerical Methods in Engineering, 2010. **83**(10): p. 1273-1311.
10. Li, B., et al., *Phase‐field modeling and simulation of fracture in brittle materials with strongly anisotropic surface energy.* International Journal for Numerical Methods in Engineering, 2015. **102**(3-4): p. 711-727.
11. Teichtmeister, S., et al., *Phase field modeling of fracture in anisotropic brittle solids.* International Journal of Non-Linear Mechanics, 2017. **97**: p. 1-21.
12. Stach, E.A., et al., *Development of a Nanoindenter for In Situ Transmission Electron Microscopy.* Microsc Microanal, 2001. **7**(6): p. 507-517.
13. Gammer, C., et al., *Local and transient nanoscale strain mapping during in situ deformation.* Applied Physics Letters, 2016. **109**(8).
14. Hÿtch, M.J. and A.M. Minor, *Observing and measuring strain in nanostructures and devices with transmission electron microscopy.* MRS Bulletin, 2014. **39**(2): p. 138-146.

15. Liu, H.H., et al., *Study of strained-silicon channel metal-oxide-semiconductor field effect transistors by large angle convergent-beam electron diffraction.* Ultramicroscopy, 2008. **108**(9): p. 816-20.
16. Chen, B., et al., *Deformation-induced phase transformation in 4H–SiC nanopillars.* Acta Materialia, 2014. **80**: p. 392-399.
17. Kiani, S., et al., *Dislocation glide-controlled room-temperature plasticity in 6H-SiC single crystals.* Acta Materialia, 2014. **80**: p. 400-406.
18. Li, X., et al., *Competing grain-boundary- and dislocation-mediated mechanisms in plastic strain recovery in nanocrystalline aluminum.* Proc Natl Acad Sci U S A, 2009. **106**(38): p. 16108-13.
19. Carlton, C.E. and P.J. Ferreira, *In situ TEM nanoindentation of nanoparticles.* Micron, 2012. **43**(11): p. 1134-9.
20. Snead, L.L., et al., *Handbook of SiC properties for fuel performance modeling.* Journal of Nuclear Materials, 2007. **371**(1-3): p. 329-377.
21. Park, K.H., et al., *Mechanical Properties of β-SiC After Si- and Dual Si + He-Ion Irradiation at Various Temperatures.* Fusion Science and Technology, 2017. **44**(2): p. 455-459.
22. Li, S., et al., *Evaluation of hardening behaviors in ion-irradiated Fe–9Cr and Fe–20Cr alloys by nanoindentation technique.* Journal of Nuclear Materials, 2016. **478**: p. 50-55.